Cell Reports, Volume *37*

Supplemental information

Distinct *in vivo* dynamics of excitatory synapses onto cortical pyramidal neurons and parvalbumin-positive interneurons

Joshua B. Melander, Aran Nayebi, Bart C. Jongbloets, Dale A. Fortin, Maozhen Qin, Surya Ganguli, Tianyi Mao, and Haining Zhong

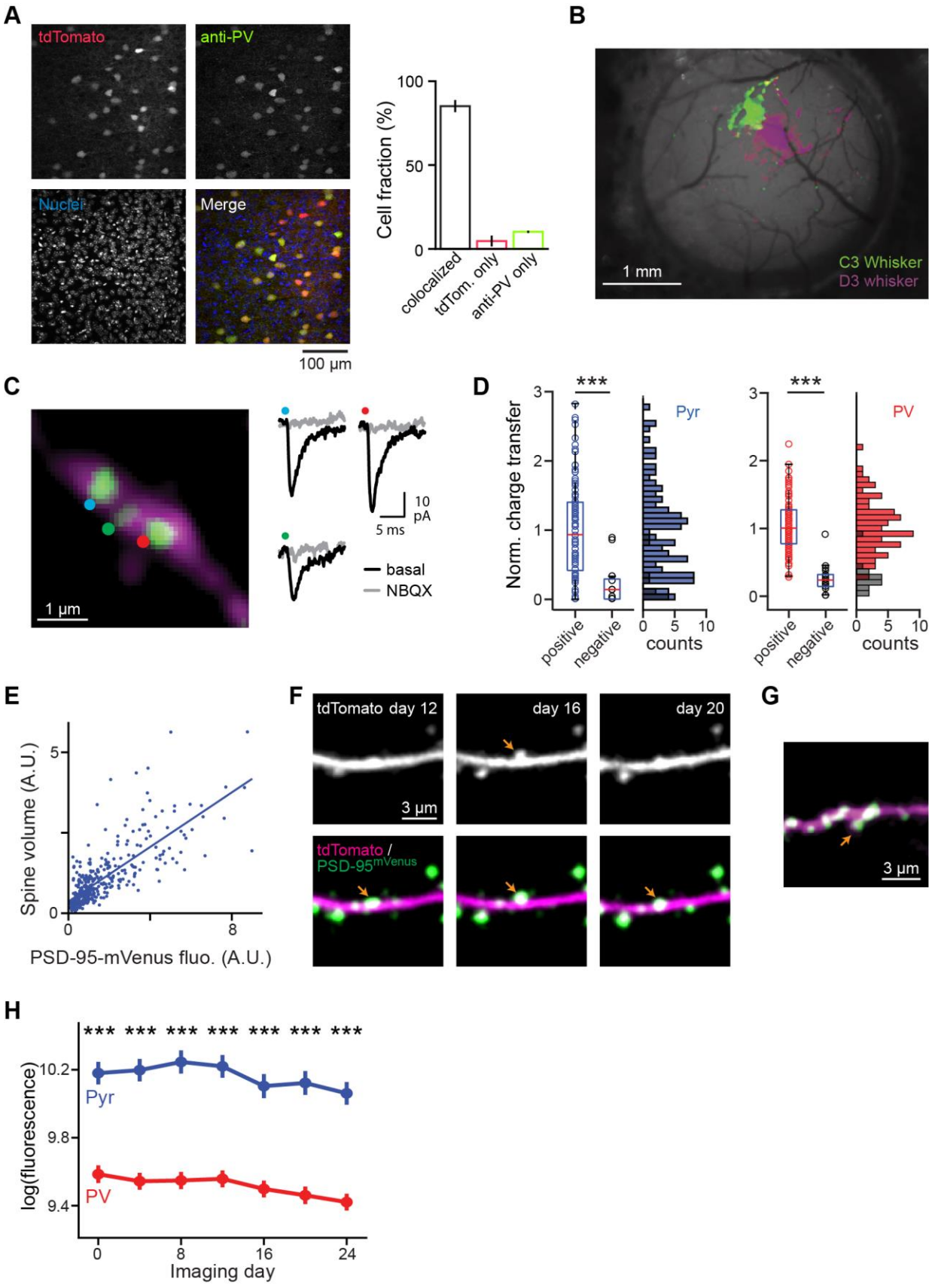
A
tdTomato
anti-PV
Nuclei
Merge
100 µm
Cell fraction (%)
100
50
0
colocalized
tdTom. only
anti-PV only
B
1 mm
C3 Whisker
D3 whisker
C
1 µm
10 pA
5 ms
basal
NBQX
D
Norm. charge transfer
***
Pyr
PV
positive
negative
counts
E
Spine volume (A.U.)
PSD-95-mVenus fluo. (A.U.)
F
tdTomato day 12
day 16
day 20
3 µm
tdTomato /
PSD-95mVenus
G
3 µm
H
*** *** *** *** *** *** ***
log(fluorescence)
10.2
9.8
9.4
Pyr
PV
Imaging day

Figure S1. Related to Figure 1. Validation and characterization of ENABLED-strategy for *in vivo* cell-type-specific targeting in the adult mouse barrel-cortex.

(A) Immunohistochemical confirmation of the *PV-IRES-Cre* driver line in the barrel cortex of adult mice. Left: example image showing tdTomato fluorescence (expressed by the *Ai9* reporter line), anti-PV labelling (via immunostaining), and nuclei (Hoescht). Right: Percentage of all cells identified by the red (tdTomato) or green (anti-PV) fluorescence alone, or colocalized. Red and green images were analyzed independently. Out of all neurons identified in both channels, 85.1% were both tdTomato-positive and PV antibody-positive. Only 4.7% of tdTomato-positive neurons lacked immune labels for the PV protein. Considering the variability associated with antibody staining, this result indicates that the PV-Cre driver line reliably labels PV+ interneurons in the barrel cortex of adult mice.

(B) Functional validation of barrel identity using intrinsic imaging in the barrel cortex. Two adjacent whiskers (C3 and D3, as indicated) were loaded into a capillary glass tube and stimulated sequentially while performing intrinsic-signal imaging. The resulting intrinsic-signal responses displayed a spatial shift that reflects the known preservation of mystacial organization in S1.

(C) NBQX blocks uEPSCs. Representative image of a PV+ neuronal dendritic stretch with PSD-95^{mVenus} puncta. Two-photon glutamate uncaging elicited uEPSCs (black lines) corresponding to the uncaging locations (colored dots) in image. The uEPSC were blocked by the AMPA receptor antagonist NBQX (gray lines).

(D) Charge transfer of uEPSC responses normalized to the averaged response of each stretch of dendrites, and their histograms, at locations with (colored circles and bars) and without (black circles and bars) PSD-95^{mVenus} puncta (see Figures 1D and 1E for examples). Glutamate uncaging at PSD-95-positive puncta yielded much higher uEPSC than locations without PSD-95 in both Pyr and PV neurons (Mann-Whitney test: for Pyr: $n_{w/\ PSD\text{-}95}$ = 101 and $n_{w/o\ PSD\text{-}95}$ = 10 uncaging spots, U = 5612, $P < 0.001$; for PV: $n_{w/\ PSD\text{-}95}$ = 75 and $n_{w/o\ PSD\text{-}95}$ = 16 uncaging spots, U = 3241, $P < 0.001$). Tukey-style boxplots represent the median (red line), first and third quartiles (box), and lowest/highest data within 1.5 times of interquartile range (whiskers). n (dendrites / cells / mice) = 9 / 6 / 3 for pyramidal neurons and 12 / 9 / 4 for PV+ neurons.

(E) Correlation of spine volume with PSD-95^{mVenus} fluorescence intensity *in vivo* for spines clearly separated from their parental dendritic shafts (n = 361 spines from 14 L2/3 pyramidal dendrites).

(F) PSD-95^{mVenus} permits the longitudinal visualization of axially-protruding spines. Representative images from three consecutive imaging sessions of a stretch of L23 pyramidal dendrite. Both morphology-only (top) and morphology with PSD-95^{mVenus} (bottom) are shown. In the morphology-only channel, a representative spine (orange arrow) can only be visualized for a single time-point; however, inclusion of the PSD-95^{mVenus} channel reveals its persistence throughout all 3 imaging sessions. This is likely the result of the spine rotating into the axial-plane and colocalizing with the dendritic shaft. Such phenomena can lead to systematic over-estimation of synaptic dynamics when using spine-morphology as the sole proxy for the presence of a synapse.

(G) Representative image of a spine (arrow) on a PV+ dendrite. Such structures were infrequently observed *in vivo*.

(H) Absolute integrated PSD-95^{mVenus} fluorescence of synapses on pyramidal and PV+ dendrites in the logarithmic scale across 7 different imaging days. Only dendrites between 10 – 50 µm beneath the pial surface were selected for this analysis to minimized depth-dependent variations in imaging conditions.

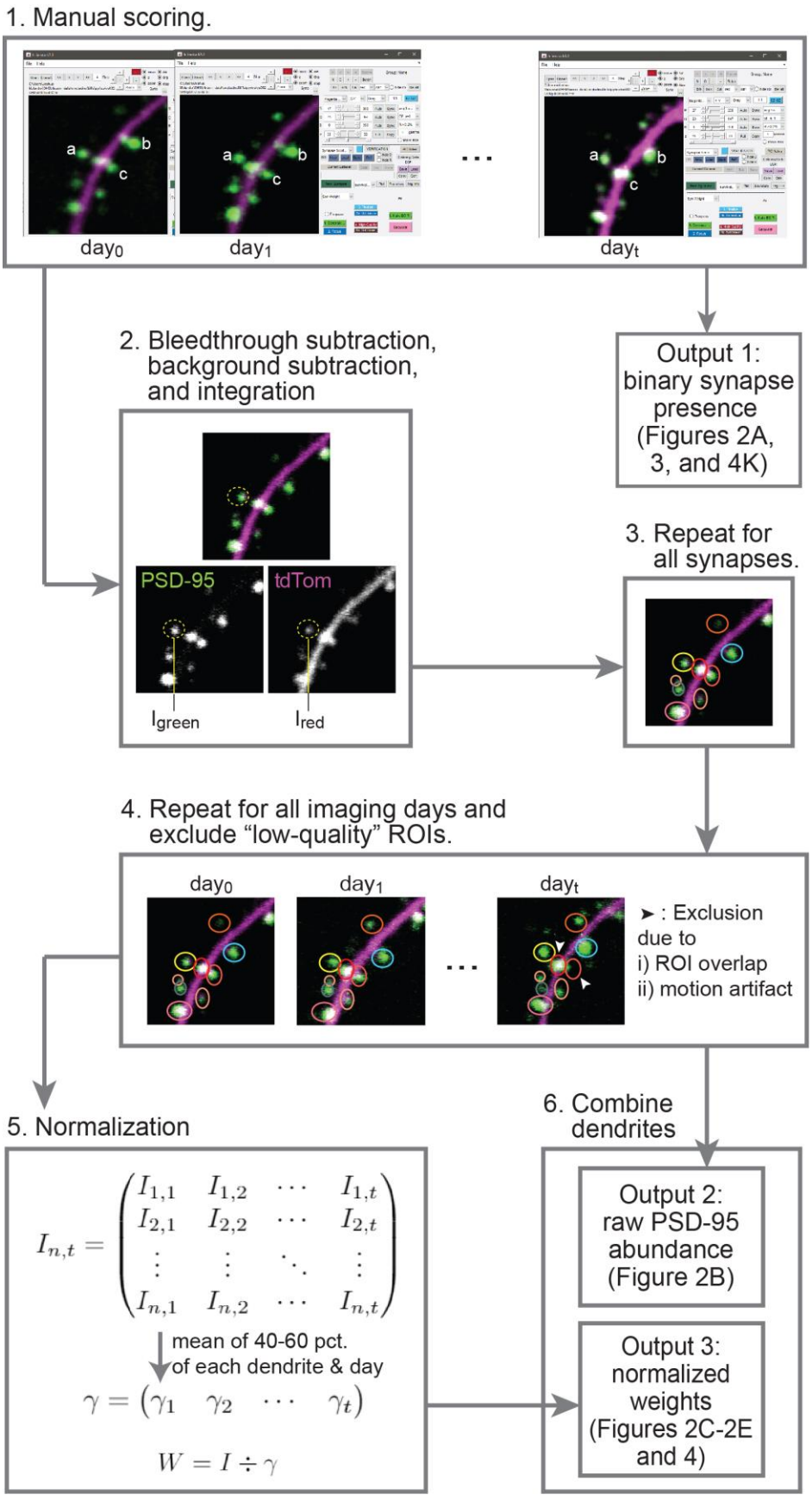
1. Manual scoring.
a
b
c
day0
day1
dayt
Output 1: binary synapse presence (Figures 2A, 3, and 4K)
2. Bleedthrough subtraction, background subtraction, and integration
PSD-95
tdTom
Igreen
Ired
3. Repeat for all synapses.
4. Repeat for all imaging days and exclude “low-quality” ROIs.
➤ : Exclusion due to
i) ROI overlap
ii) motion artifact
5. Normalization
$I_{n,t} = \begin{pmatrix} I_{1,1} & I_{1,2} & \cdots & I_{1,t} \\ I_{2,1} & I_{2,2} & \cdots & I_{2,t} \\ \vdots & \vdots & \ddots & \vdots \\ I_{n,1} & I_{n,2} & \cdots & I_{n,t} \end{pmatrix}$
mean of 40-60 pct. of each dendrite & day
$\gamma = \begin{pmatrix} \gamma_1 & \gamma_2 & \cdots & \gamma_t \end{pmatrix}$
$W = I \div \gamma$
6. Combine dendrites
Output 2: raw PSD-95 abundance (Figure 2B)
Output 3: normalized weights (Figures 2C-2E and 4)

Figure S2. Related to Figures 2, 3 and 4. Schematic data analysis pipeline.

(1) We developed a custom MATLAB GUI and accompanying post-processing software to manually score synaptic identity over an arbitrary number of time points and extract integrated fluorescence values from those synapses. Image exploration across time and x, y, and z dimensions was facilitated by easy-to-use keyboard and mouse controls. To minimize scoring errors, synapses were scored one-at-a-time starting with first appearance, with a mechanism to bring the user's cursor to the same X-Y coordinate at each subsequent time point (to facilitate the identification of a given synapse). Puncta could be classified as protruding on a spine or colocalizing with the dendritic shaft, or flagged to indicate that the scorer was unsure about the identity of a given synapse on a given day. Finalizing the scoring for a dendrite required the user to "verify" that dendrite by scanning through each scored segment of a time series to ensure that no synapses were missed. (2, 3, and 4) Elliptical ROIs were generated and manually sized around each synapse. The size of the ROI was held constant across time points for a given synapse. The pixel values from within the ROIs were integrated for both green and red channels, after performing bleedthrough subtraction, which corrects for the small amount of tdTomato signal detected in the green channel (2%), and background subtraction. Puncta that appeared blurred due to motion artifact, or were too close to neighboring puncta to resolve, were flagged within the software and excluded from analyses that depended on fluorescent intensity (but not the binary presence of synapses, such as density and survival fraction). (5) Integrated fluorescent values of individual puncta for each time point were normalized by the average of the 40^{th} – 60^{th} percentile of all values for that day (γ), in order to correct for differences in imaging

conditions from day-to-day. (6) The normalized matrices (*W*) of integrated fluorescence (“weights”) from all dendrites were concatenated for each condition (Pyr and PV+).

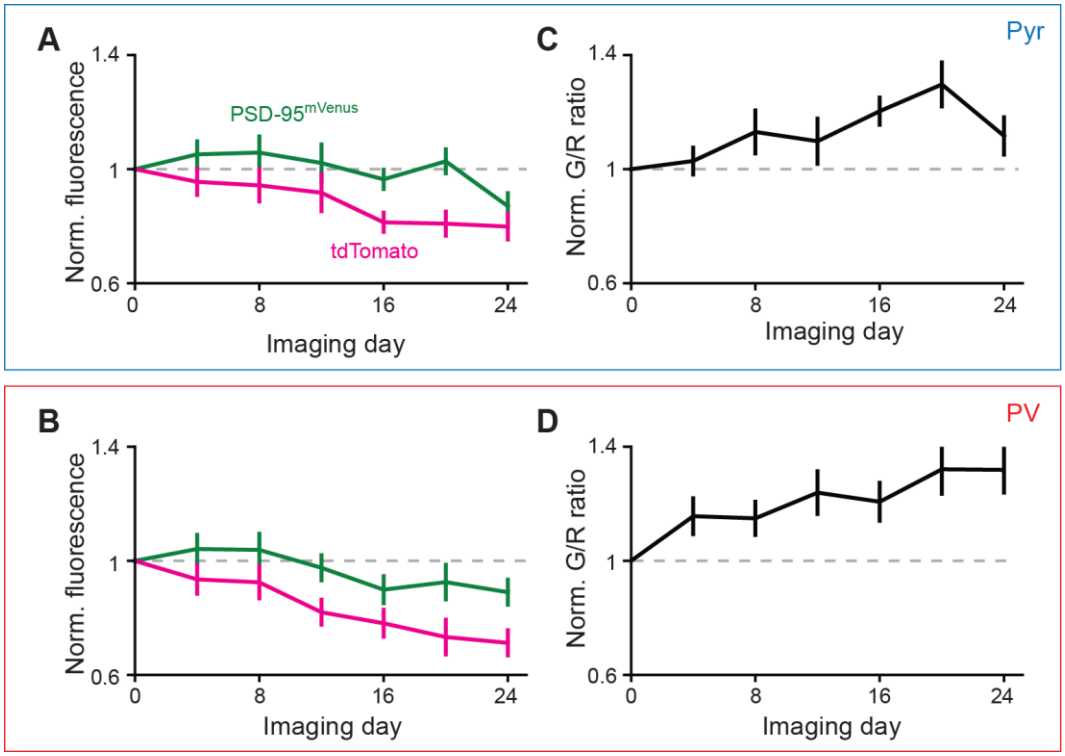

Figure S3. Related to Figure 3. TdTomato and PSD-95^{mVenus} proteins are differentially bleached.

(A, B) Time course of the average (40th to 60th percentile) raw PSD-95^{mVenus} and tdTomato fluorescence values on L23 pyramidal dendrites (A) and PV+ dendrites (B) *in vivo*, normalized to the average raw-values on the first day of imaging.

(C, D) Time course of the average (40th to 60th percentile) green-to-red ratio of puncta on L23 pyramidal dendrites (C) and PV+ dendrites (D) *in vivo*, normalized to the average green-to-red ratio on the first day of imaging.

Note: the accumulated bleaching of cytosolic tdTomato and PSD-95^{mVenus} is not equivalent. tdTomato fluorescence attenuated more rapidly. These data suggest that

the green-to-red ratio of a given synapse, as a normalized quantification of green intensity, is prone to artifact.

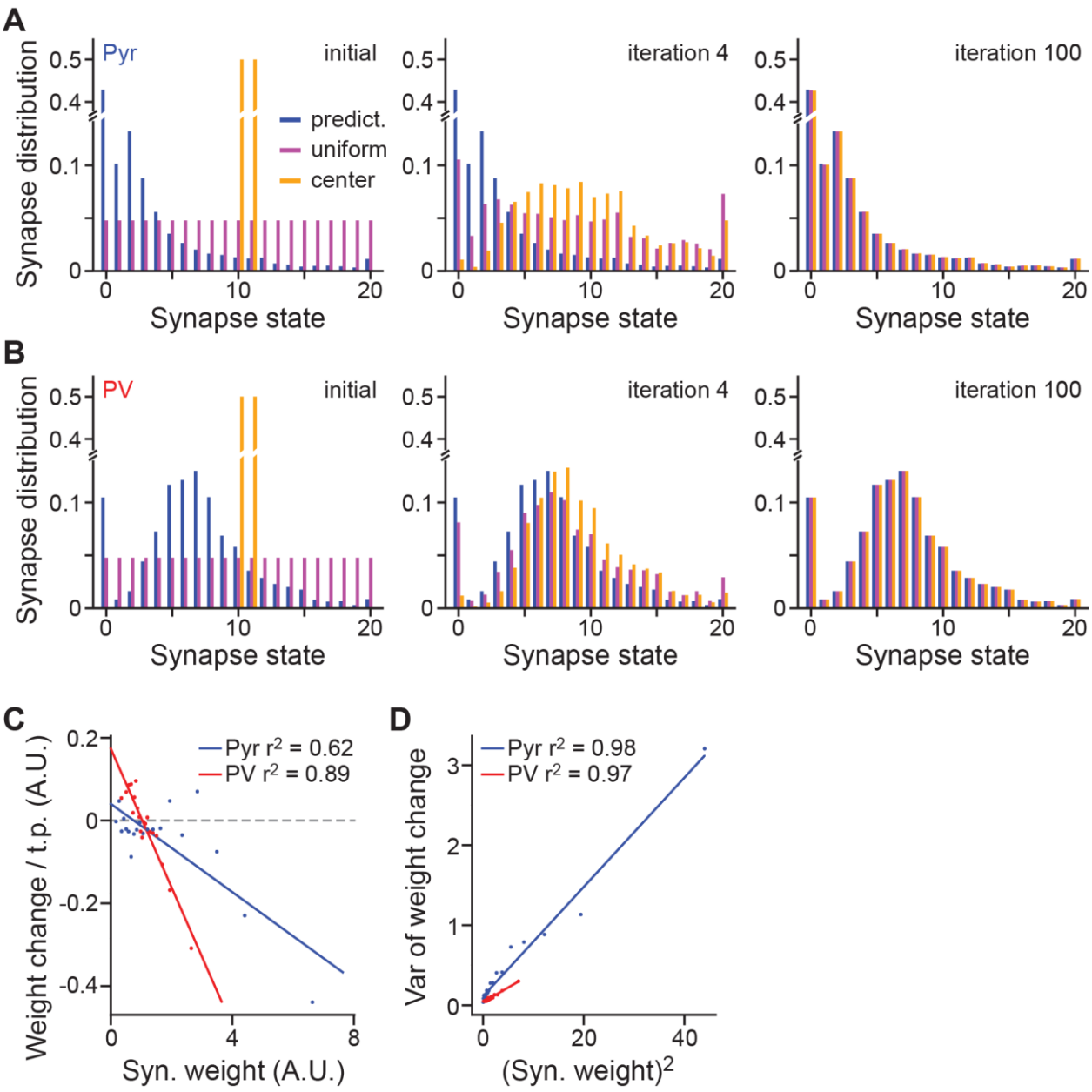

Figure S4. Related to Figure 4. Synaptic weight dynamics are cell type-specific and determine the steady state synaptic weight distribution.

(A, B) The evolution of three different starting distributions for Pyr (A) and PV+ (B) synapses by iterating through the corresponding Markovian transition matrix, as illustrated in Figures 4C and 4D. Three distributions were tested for each neuronal type:

1) the predicted steady state distribution of the fit Markov chain (blue), 2) a hypothetical “center” distribution in which all synaptic weights are assigned to the center two states (orange), and 3) a uniform distribution across states (magenta) are included. The predicted steady distributions of both neuronal type did not change significantly over iterations, but the two hypothetical distributions gradually evolved and converged to mimic the corresponding predicted steady state distribution.

(C) For each cell type, synaptic strengths were binned into 20 bins with equal counts. A line to the average (within bins) consecutive weight changes $w_{t+1} – w_t$ was fit using the average synaptic weight $<w_t>$ as input (See **STAR METHODS*Kesten Model*** for details). Following the framework of *Ziv and Brenner*, 2018 that describes weight-dynamics as a combination of additive and weight-dependent multiplicative changes, these data suggest that excitatory synapses on PV+ dendrites have a stronger additive component in their dynamics than those on L23 pyramidal dendrites.

(D) Same as C, but the variance of the consecutive weight changes $w_{t+1} – w_t$ was fit using the square of the average synaptic weight $<w_t>^2$ as input.

Pyr dendrites					
animal ID	Dendrite ID	length	num_syn	num_hq_syn	sex
ai	3	38.36861	41	30	Male
ai	10	30.76077	36	31	Male
be	3	33.78513	52	49	Female
be	5	49.9705	70	53	Female
cs	2	32.67719	60	30	Male
cs	3	45.62966	62	52	Male
cs	5	44.86299	53	51	Male
cs	6	42.51104	66	56	Male
cs	7	34.46618	53	51	Male
ct	1	49.34215	44	40	Male
ct	3	47.29193	83	71	Male
ct	7	39.18292	53	50	Male
ct	8	39.23189	76	59	Male
ct	10	46.93612	60	55	Male
total		575.0171	809	678	
average		41.07265	57.78571	48.42857	
s.e.m.		6.47873	13.18611	11.84979	
PV dendrites					
animal ID	Dendrite ID	length	num_syn	num_hq_syn	sex
ah	1	40.12993	43	28	Male
ah	2	27.80366	25	12	Male
ah	7	29.53844	32	23	Male
ak	9	26.80679	25	15	Male
ak	11	48.23904	41	35	Male
br	1	48.48825	41	23	Female
br	7	34.11306	32	21	Female
br	10	30.7584	29	22	Female
cq	1	36.45706	34	29	Male
cq	2	38.85113	37	9	Male
cq	4	43.1545	37	17	Male
cq	6	28.11853	30	18	Male
cq	11	34.51986	37	25	Male
cr	2	38.27673	31	14	Male
cr	4	52.37804	46	39	Male
cv	3	41.47919	38	22	Female
cv	6	36.87302	39	29	Female

cv	7	35.4692	34	22	Female
cv	9	40.53846	37	15	Female
cv	11	45.64533	43	22	Female
dh	10	27.65974	28	11	Female
total		785.2984	739	451	
average		37.39516	35.19048	21.47619	
s.e.m.		7.476379	5.946588	7.717636	

Supplemental Table S1. Related to Figures 2, 3, and 4. Dendrite information.